A Non-Quasi-Static MOSFET Model for SPICE—AC Analysis

Hong June Park, *Member, IEEE*, Ping Keung Ko, *Member, IEEE*, and Chenming Hu, *Fellow, IEEE*

***Abstract*—Based on an approximate solution to the nonlinear current continuity equation in the channel, an analytic non-quasi-static model for long channel MOSFET's has been derived and implemented in SPICE. The model includes the large-signal transient and the small-signal ac analyses, although only the ac model is reported in this paper. Excellent agreement in simulation results has been achieved between this work and CODECS (a mixed device and circuit simulator) [1]. The CPU time required for this work is about twice as long as that for currently available quasi-static (QS) MOSFET models in SPICE.**

Nomenclature

W	Effective channel width of a MOSFET.
L	Effective channel length of a MOSFET.
C_{OX}	Gate oxide capacitance per unit area.
N_{SUB}	Substrate doping concentration.
q	An electronic charge ($1.602 \cdot 10^{-19}$ C).
γ	Bulk effect coefficient ($\sqrt{2\epsilon_{si} q N_{SUB}}/C_{OX}$).
y	Lateral dimension along the channel from source ($y = 0$) toward drain ($y = L$).
y'	Normalized lateral dimension (y/L).
I_y	Total (dc + ac) channel current at y.
i_y	AC small-signal phasor of I_y.
μ_0	Mobility of channel carriers.
Q_n	Total (dc + ac) channel charge density.
Q_n'	Normalized total channel charge density, $-Q_n/(WC_{OX})$.
Ψ_{SO}	Surface potential at the source end ($y = 0$) of channel.
Ψ_{SL}	Surface potential at the drain end ($y = L$) of channel.
k	Boltzmann constant.
T	Temperature in degree kelvin.
V_t	Thermal voltage (kT/q).
D_n	Diffusion constant of channel carriers ($\mu_0 \cdot kT/q$).
V_{FB}	Flat-band voltage.
V_{TH}	Threshold voltage in conventional notation.
V_{DSSAT}	Drain saturation voltage.
V_{GST}	($V_{GS} - V_{TH}$) in conventional notation.
F_B	Body factor as defined in [2, eq. (5)].
$P(y, t)$	$(Q_n'(y, t) + F_B V_t)^2$.
P_S	Value of $P(y, t)$ at the source end ($y = 0$) of channel, [2, eq. (13)].
P_D	Value of $P(y, t)$ at the drain end ($y = L$) of channel [2, eq. (14)].
V_{GB}	Total (dc + ac) gate-to-bulk voltage.
V_{GS}	Total (dc + ac) gate-to-source voltage.
V_{DS}	Total (dc + ac) drain-to-source voltage.
V_G, V_D, V_S, V_B	Gate, drain, source, and bulk node voltages, respectively, at dc operating point.
v_g, v_d, v_s, v_b	AC small-signal phasors of the gate, drain, source, and bulk node voltages, respectively.
v_{gs}	AC small-signal phasor of the gate-to-source voltage.
v_{bs}	AC small-signal phasor of the bulk-to-source voltage.
ω	Signal angular frequency ($2\pi f$).
ω_T	Critical angular frequency defined in (4.c).
f_T	$\omega_T/(2\pi)$.
τ_T	Channel transit time, ($1/\omega_T$), (4.c).
$\alpha(\omega)$	Normalized complex frequency defined in (4.b).
$p(y, \omega)$	AC small-signal phasor of $P(y, t)$ at frequency ω.
$p_s(\omega)$	$p(y, \omega)$ at the source end of channel.
$p_d(\omega)$	$p(y, \omega)$ at the drain end of channel.
r	Asymmetry factor which is 1 in the saturation region and is 0 when $V_{DS} = 0$, see (2.c).
b_1, b_2	Equations (A2.1), (A2.2).
d_1, d_2	Equations (A2.3), (A2.4).
B, C, E	Equations (A2.5), (A2.6), (A2.7).
G, H	Equations (A2.8), (A2.9).
I_{DC}	DC drain current defined in (10.a).

Manuscript received September 11, 1990; revised December 31, 1991. This work was supported in part by SRC, INTEL, and California State MICRO. This paper was recommended by Associate Editor A. Ruehli.

H. J. Park was with the University of California at Berkeley. He is now with Pohang Institute of Science and Technology, Pohang, Kyungbuk, South Korea.

P. K. Ko and C. Hu are with the Department of Electrical Engineering and Computer Sciences, University of California at Berkeley, Berkeley, CA 94720.

IEEE Log Number 9200819.

0278-0070/92$03.00 © 1992 IEEE

$i_d(\omega)$ AC small-signal phasor of drain current, see (9.a).
$i_s(\omega)$ AC small-signal phasor of source current, see (9.b).
$i_g(\omega)$ AC small-signal phasor of gate current.
$i_b(\omega)$ AC small-signal phasor of bulk (substrate) current.
β_p $(W/L) \cdot C_{OX} \cdot \mu_0/(2F_B)$.
λ Channel length modulation factor, see (10.a).
$\{\omega_{p \cdot n}\}$ Angular frequencies in (14.a) and (14.b), where $n = 1, 2, 3, 4, \cdots$.
$\{\omega_{z \cdot n}\}$ Angular frequencies in (14.b), where $n = 1, 2, 3, 4, \cdots$.
$\omega_{3\text{-dB}}$ 3-dB frequency of i_d in the saturation region, see (18).
δ AC small-signal channel current partitioning ratio, see (19).
q_d AC small-signal phasor of the drain charge.
q_s AC small-signal phasor of the source charge.
g_m Small-signal transconductance $(\partial i_d/\partial v_{gs})$ at dc $(\omega = 0)$.
g_{mbs} Small-signal transconductance $(\partial i_d/\partial v_{bs})$ at dc $(\omega = 0)$.
g_{ds} Small-signal conductance $(\partial i_d/\partial v_{ds})$ at dc $(\omega = 0)$.
cgdo Gate to drain overlap capacitance per unit channel width.
cgso Gate to source overlap capacitance per unit channel width.
cj Bottom junction capacitance per unit area.
cjsw Sidewall junction capacitance per unit length.
C_{OVD} Gate-to-drain overlap capacitance, $(cgdo \cdot W)$.
C_L Load capacitance including junction capacitance.
C_{BG} Quasi-static bulk-to-gate capacitance, $\partial Q_B/\partial V_G$.
C_{BB} Quasi-static bulk-to-bulk capacitance, $\partial Q_B/\partial V_B$.
C_{BD} Quasi-static bulk-to-drain capacitance, $\partial Q_B/\partial V_D$.
C_{BS} Quasi-static bulk-to-source capacitance, $\partial Q_B/\partial V_S$.

I. Introduction

MOSFET'S have been widely used in analog circuits as well as in digital circuits [3], and circuit simulation programs, such as SPICE, have been used extensively to predict the circuit performance. Initially, Meyer's MOSFET capacitance model [4] was implemented in SPICE and it has widely been used for MOSFET circuit simulations. Lately charge based MOSFET capacitance models were invented and implemented in SPICE [5]–[7]. According to channel charge partitioning schemes, they are grouped into quasi-static (QS) 40/60 [5], [6] and QS 0/100 [7] models, etc. The ratios 40/60 and 0/100 refer to the ratios of drain and source charges in the saturation region.

For digital applications, the above-mentioned QS MOSFET capacitance models are adequate, since at high frequencies, intrinsic MOSFET capacitance components are overwhelmed by the extrinsic capacitances such as overlap, junction, and interconnect capacitances. On the other hand, for analog applications, sometimes long-channel MOSFET's may be used with the operating point of the gate voltage set just above the threshold voltage to achieve high dc gain. Hence, the effect of intrinsic MOSFET capacitances becomes important for simulating high frequency analog MOSFET circuits, for example, for predicting phase margins of wide-band amplifiers [8].

Therefore, both the Meyer model and the charge based models are not adequate for high frequency analog MOSFET circuit simulations. This is due to the fact that both the Meyer model and the charge-based QS models are derived based on the QS assumption, that is, neglecting the transmission line effect. Hence, non-QS MOSFET models are required for accurate simulation of high frequency analog MOSFET circuits, as suggested by several researchers [5], [8]–[14].

Burns [15], Das [16], and Treleaven *et al.* [17] analyzed the transmission line effect of long-channel MOSFET's and derived current equations. Bagheri *et al.* [10] revisited this problem and derived ac node current equations, including the substrate effects, using the iterative solution of the current continuity equation. At the submission of this paper, Roblin *et al.* reported analytic solution for velocity-saturated wave equation and its application to MODFET [18].

In this work, simple analytic equations have been derived for ac node currents, implemented in SPICE, and the simulation results are compared with CODECS (a mixed device and circuit simulator) [1] and other currently available QS MOSFET models in SPICE.

The counterpart of this paper for transient analysis was reported in [2]. Since the initial portion of model derivation steps is the same for this paper and [2], to save space it is not shown here.

II. Formulation of Model Equations

From the current continuity equation and the current relation, one can derive

$$\frac{\partial P(y, t)}{\partial t} = D(y, t) \cdot \frac{\partial^2 P(y, t)}{\partial y^2} \tag{1.a}$$

where

$$P(y, t) = (Q_n'(y, t) + F_B V_t)^2 \tag{1.b}$$

$$D(y, t) = \frac{\mu_0}{F_B} \cdot (Q_n'(y, t) + F_B V_t) = \frac{\mu_0}{F_B} \cdot \sqrt{P(y, t)} \tag{1.c}$$

where $Q_n'(y, t)$ is the inversion charge density profile normalized by WC_{OX}, y is the lateral dimension from source ($y = 0$) toward drain ($y = L$) as shown in Fig. 1 of [2], and F_B is the body factor. The derivation steps of (1.a)–(1.c) and approximations involved are shown in the counterpart of this paper for transient analysis [2].

To solve the second-order differential equation (1.a), one can establish two boundary conditions for $P(y, t)$, $P_S(t)$, and $P_D(t)$, at the source and drain ends of the channel, respectively, by assuming that the carrier densities at those end positions respond instantaneously to the applied bias. Equations for F_B, $P_S(t)$, and $P_D(t)$ can be found in [2, (5), (13), (14)] respectively. To derive the approximation equation for F_B in [2, (5)], the strong inversion surface potential, $(2\Phi_F - V_{BS}(t))$, in the F_B equation of [25] is replaced by $\Psi_{SO}(t)$ in this work to extend the usage of F_B to the weak inversion region. The F_B equation of [25] was originally derived by Poon [19], but the coefficients of the approximation are slightly different. Derivation steps of the F_B approximation in [19] and [25] are also shown in [20] and [21], respectively. Other approximations of F_B can be found in [22].

For the small-signal ac analysis, the QS value is used for the diffusion coefficient $D(y, t)$ in (1.c). This can be justified by assuming that the small-signal ac component of $(Q_n'(y, t) + F_B V_t)$ in (1.c) is much smaller than the QS dc component. The QS component of $(Q_n'(y, t) + F_B V_t)$ can be computed from eq. (8) of [2] with the time derivative set of 0.

$$D(y, t) = D(0, t) \cdot \sqrt{1 - r \cdot \frac{y}{L}} \tag{2.a}$$

where

$$D(0, t) = \frac{\mu_0}{F_B} \cdot (V_{GST}(t) + F_B V_t) \tag{2.b}$$

$$r = 1 - \frac{P_D}{P_S}. \tag{2.c}$$

For the ac sinusoidal excitation, we decompose $P(y, t)$ into the dc component and the small-signal ac component. The dc component of $P(y, t)$ can be derived from (1.a) with the time derivative set to 0:

$$P(y, t) = P_S + (P_D - P_S) \cdot \frac{y}{L} + p(y, \omega) \cdot e^{j\omega t} \tag{3}$$

where P_S and P_D are dc values of $P(y, t)$ at source and drain ends, respectively, and $p(y, \omega)$ is the ac small-signal phasor profile.

Throughout this paper, upper case letters represent dc operating point quantities and lower case letters represent ac small-signal phasor quantities, unless they are specified otherwise.

Substitution of (3) into (1.a) gives

$$\alpha^2(\omega) \cdot p(y', \omega) = \frac{\partial^2 p(y', \omega)}{\partial y'^2} \cdot \sqrt{1 - r \cdot y'} \tag{4.a}$$

where

$$\alpha(\omega) = \sqrt{j \frac{\omega}{\omega_T}} = (1 + j) \cdot \sqrt{\frac{\omega}{2\omega_T}} \tag{4.b}$$

$$\omega_T = \frac{\mu_0}{L^2} \cdot \left(\frac{V_{GST}}{F_B} + V_t\right) = \frac{1}{\tau_T} \tag{4.c}$$

where $y' = y/L$ and τ_T is the channel transit time including the diffusion term $(F_B V_t)$. ω_T is determined by the dc operating point as shown in (4.c).

If $r = 0$, the exact solutions to (4.a) are $e^{\alpha(\omega)y'}$ and $e^{-\alpha(\omega)y'}$. To model the effect of $\sqrt{1 - r \cdot y'}$ in (4.a) for nonzero r, the solution for $p(y', \omega)$ is assumed to be exponential function times polynomial in y' as shown in (5). For the compromise of accuracy and computational cost, only second-order polynomials are used. In the early version of this paper briefly described in [23], only a first-order polynomial is used. It has been changed to second-order polynomial in this work to match CODECS [1] simulation results more closely.

$$\begin{aligned} p(y', \omega) = {} & G(\omega) \cdot e^{\alpha(\omega)y'} \\ & \cdot (1 + b_1(\omega) \cdot y' + b_2(\omega) \cdot y'^2) \\ & + H(\omega) \cdot e^{-\alpha(\omega)y'} \\ & \cdot (1 + d_1(\omega) \cdot y' + d_2(\omega) \cdot y'^2). \end{aligned} \tag{5}$$

The equations for the coefficients $b_1(\omega)$, $b_2(\omega)$, $d_1(\omega)$, $d_2(\omega)$, $G(\omega)$, and $H(\omega)$ and their derivation steps are shown in Appendix II.

Substituting the equations in Appendix II into (5), the ac small-signal phasor profile $p(y', \omega)$ can be rewritten as

$$p(y', \omega) = \frac{\left[\begin{aligned} & p_s(\omega) \cdot \left\{\begin{aligned} & ((C - B)(C - By') + (B - E)(E - By'^2)\alpha^2) \cdot \sinh(\alpha(1 - y')) \\ & + B \cdot ((C - E) - (B - E)y' - (C - B)y'^2) \cdot \alpha \cdot \cosh(\alpha(1 - y')) \end{aligned}\right\} \\ & + p_d(\omega) \cdot \{(C(C - By') - E(E - By'^2)\alpha^2) \cdot \sinh(\alpha y') + B(-Ey' + Cy'^2) \cdot \alpha \cdot \cosh(\alpha y')\} \end{aligned}\right]}{(C(C - B) + E(B - E)\alpha^2) \cdot \sinh\alpha + B(C - E) \cdot \alpha \cdot \cosh\alpha} \tag{6}$$

where equations for B, C, and E are shown in Appendix II. Although (6) looks complex, one can observe that $p(y', \omega)$ is linear in y' at $\omega = 0$ and $p(y', \omega)$ at very high

frequencies ($\omega >> \omega_T$) is reduced to two exponential tails which are nonzero only near the drain and source ends, respectively [24].

The phasors $p_s(\omega)$ and $p_d(\omega)$ can be found by using the derivatives of P_D and P_S in [2, eqs. (13) and (14)] with respect to applied biases:

$$p_s(\omega) = \frac{\partial P_S}{\partial V_G} \cdot v_g(\omega) + \frac{\partial P_S}{\partial V_B} \cdot v_b(\omega) + \frac{\partial P_S}{\partial V_D} \cdot v_d(\omega) + \frac{\partial P_S}{\partial V_S} \cdot v_s(\omega) \tag{7.a}$$

$$p_d(\omega) = \frac{\partial P_D}{\partial V_G} \cdot v_g(\omega) + \frac{\partial P_D}{\partial V_B} \cdot v_b(\omega) + \frac{\partial P_D}{\partial V_D} \cdot v_d(\omega) + \frac{\partial P_D}{\partial V_S} \cdot v_s(\omega) \tag{7.b}$$

where $v_g(\omega)$, $v_b(\omega)$, $v_d(\omega)$ and $v_s(\omega)$ are the small-signal phasors at each node, respectively. Eqs. (7.a) and (7.b) are based on the assumption that the small-signal excitations at source and drain ends follow the applied bias instantaneously.

Using [2, eq. (6)], (1.b), and (3), the small-signal channel current, $i_y(y', \omega)$, can be written as

$$i_y(y', \omega) = \frac{W}{L} \cdot C_{OX} \cdot \frac{\mu_0}{2F_B} \cdot \frac{\partial p(y', \omega)}{\partial y'}. \tag{8}$$

From (6) and (8), the ac small-signal drain and source currents can be written as

$$i_d(\omega) = \frac{W}{L} \cdot C_{OX} \cdot \frac{\mu_0}{2F_B} \cdot \frac{p_s \cdot (((C^2 - BE) - (B - E)^2 \cdot \alpha^2) \cdot \alpha) - p_d \cdot ((-BC + B(3E - C) \cdot \alpha^2) \cdot \sinh \alpha + (C^2 - BE + BC + E(B - E) \cdot \alpha^2) \cdot \alpha \cosh \alpha)}{(C(C - B) + E(B - E) \cdot \alpha^2) \cdot \sinh \alpha + B(C - E) \cdot \alpha \cdot \cosh \alpha} \tag{9.a}$$

$$i_s(\omega) = -\frac{W}{L} \cdot C_{OX} \cdot \frac{\mu_0}{2F_B} \cdot \frac{p_s \cdot ((B(C - B) + B(C - E) \cdot \alpha^2) \cdot \sinh \alpha + (B(B - E) + C(C - B) + E(B - E) \cdot \alpha^2) \cdot \alpha \cdot \cosh \alpha) - p_d \cdot ((C^2 - BE - E^2 \cdot \alpha^2) \cdot \alpha)}{(C(C - B) + E(B - E) \cdot \alpha^2) \cdot \sinh \alpha + B(C - E) \cdot \alpha \cdot \cosh \alpha} \tag{9.b}$$

In (9.a) and (9.b), the ω dependences of α, p_s, and p_d are not shown for simplicity. The dc drain current equation, including the empirical channel length modulation effect, can be derived as

$$I_{DC} = \beta_p \cdot (P_S - P_D) \cdot (1 + \lambda V_{DS}) \tag{10.a}$$

where

$$\beta_p = \frac{W}{L} C_{OX} \frac{\mu_0}{2F_B} \tag{10.b}$$

λ in (10.a) is a constant. A simple model is used for the channel length modulation effect in this paper to concentrate on the non-QS behavior.

The non-QS component in the ac small-signal bulk current $i_b(\omega)$ is neglected. Hence $i_b(\omega)$ is derived using the QS approximation as

$$i_b(\omega) = j\omega \cdot (C_{BG} \cdot v_g(\omega) + C_{BB} \cdot v_b(\omega) + C_{BD} \cdot v_d(\omega) + C_{BS} \cdot v_s(\omega)) \tag{11}$$

C_{BG}, C_{BB}, C_{BD}, and C_{BS} in (11) are QS bulk capacitances, which are functions of node voltages only and are independent of the signal angular frequency ω. The ac small-signal gate current is derived from

$$i_g(\omega) = -(i_d(\omega) + i_s(\omega) + i_b(\omega)) \tag{12}$$

For the ac analysis in SPICE, we need the derivatives of ac small-signal currents, i_d, i_s, i_g, and i_b with respect to ac node voltages, which are used to construct the linearized ac small-signal equivalent circuit. These derivatives can be derived by using the chain rule [24].

III. AC Model in the Saturation Region

A. NQS AC Model in the Saturation Region

For the ac analysis of MOSFET's we are interested mostly in the saturation region, where the voltage gain is high. For the high frequency MOS circuits, we are interested in the intrinsic behavior of MOSFET's at high frequencies [8]. To see the intrinsic behavior of MOSFET's we neglect the extrinsic components such as the overlap capacitance and the source, drain junction capacitance.

In the saturation region, the factor r in (2.c) is 1 and p_d is 0 (no velocity saturation effect included) and the small-signal drain and source current equations in (9.a) and (9.b) are reduced to

$$i_d(\omega) = \beta_p p_s(\omega) \cdot \frac{\alpha \cdot (1 - 0.014248\alpha^2)}{(0.77111 + 0.016920\alpha^2) \cdot \sinh \alpha + 0.22889 \cdot \alpha \cdot \cosh \alpha} \tag{13.a}$$

$$i_s(\omega) = -\beta_p p_s(\omega) \cdot \frac{(0.19772 + 0.22889\alpha^2) \cdot \sinh \alpha + (0.80228 + 0.016920\alpha^2) \cdot \alpha \cdot \cosh \alpha}{(0.77111 + 0.016920\alpha^2) \cdot \sinh \alpha + 0.22889 \cdot \alpha \cdot \cosh \alpha}. \tag{13.b}$$

In this derivation the channel length modulation effect is not included.

Expanding sinh α and cosh α in (13.a) and (13.b) as Taylor series in α, we can represent i_d and i_s as rational functions of s, where $s = j\omega = \alpha^2 \cdot \omega_T$ and α is shown in (4.b).

$$i_d(\omega) = \beta_p \cdot p_s(\omega) \cdot \frac{1 - \dfrac{s}{70.185\omega_T}}{1 + \sum_{n=1}^{\infty} \left(\dfrac{s}{\omega_{p \cdot n}}\right)^n} \quad (14.a)$$

$$i_s(\omega) = -\beta_p \cdot p_s(\omega) \cdot \frac{1 + \sum_{n=1}^{\infty} \left(\dfrac{s}{\omega_{z \cdot n}}\right)^n}{1 + \sum_{n=1}^{\infty} \left(\dfrac{s}{\omega_{p \cdot n}}\right)^n} \quad (14.b)$$

The first five values of $\{\omega_{p \cdot n}/\omega_T\}$ and $\{\omega_{z \cdot n}/\omega_T\}$ are shown in Table I.

The Taylor series expansion (14.a) shows that all the coefficients of s terms in the denominator are positive and so i_d has infinitely many *poles* in the left-hand side of the s-plane. Similarly, i_s in (14.b) has infinitely many *zeros* in the left-hand side of the s-plane. The *poles* of i_s are the same as those of i_d.

At low frequencies ($\omega < \omega_T$), (13.a) and (13.b) are reduced to

$$i_d(\omega) \approx \beta_p p_s(\omega) \left\{ 1 - \frac{j0.27413 \cdot \dfrac{\omega}{\omega_T}}{1 + j0.25988 \cdot \dfrac{\omega}{\omega_T}} \right\} \quad (15.a)$$

$$i_s(\omega) \approx \beta_p p_s(\omega) \left\{ -1 - \frac{j0.42002 \cdot \dfrac{\omega}{\omega_T}}{1 + j0.25988 \cdot \dfrac{\omega}{\omega_T}} \right\}. \quad (15.b)$$

Equations (15.a) and (15.b) may be useful for hand calculations.

$\beta_p \cdot p_s$ in the saturation region can be rewritten as

$$\beta_p \cdot p_s(\omega) = g_m \cdot v_{gs}(\omega) + g_{mbs} \cdot v_{bs}(\omega) \quad (16)$$

where v_{gs} and v_{bs} are the ac small-signal phasors of the gate to source voltage and the bulk to source voltage, respectively, and g_m and g_{mbs} are the dc transconductances and can be approximated in the saturation region as

$$g_m \approx \frac{W}{L} \cdot C_{OX} \cdot \frac{\mu_0}{F_B} \cdot (V_{GST} + F_B \cdot V_t) \quad (17.a)$$

$$g_{mbs} \approx g_m \cdot \left(-\frac{\partial V_{TH}}{\partial V_{BS}}\right) \quad (17.b)$$

where V_{TH} is the conventional threshold voltage.

TABLE I
THE FIRST 5 VALUES OF COEFFICIENTS $\{\omega_{p \cdot n}\}$, $\{\omega_{z \cdot n}\}$ IN (14a) AND (14b)

n	1	2	3	4	5
$\frac{\omega_{p \cdot n}}{\omega_T}$	3.8479	7.2966	11.779	17.302	23.871
$\frac{\omega_{z \cdot n}}{\omega_T}$	1.4708	3.4989	6.4275	10.285	15.094

B. Frequency Responses of AC Small-Signal Drain and Source Currents in the Saturation Region

Frequency responses of intrinsic ac small-signal drain and source currents i_d and i_s in the saturation region are shown in Table II for this paper and QS models. Extrinsic current components, that is, currents through the extrinsic capacitors such as overlap and junction capacitors, are not included.

Fig. 1 shows the in-phase (real) and the out-of-phase (imaginary) components of i_d in the saturation region with respect to the normalized frequency. i_d is normalized by the dc value $\beta_p p_s$. ac signal is applied at the gate node. All the QS models show that the in-phase component of i_d is constant independent of frequency, but this paper and CODECS [1] show that the in-phase component of i_d decreases in magnitude with frequency and goes asymptotically to 0 at very high frequencies.

CODECS is a mixed device and circuit simulator which uses two-dimensional device simulation to compute the node currents.

The QS 0/100 and Meyer model show that the out-of-phase component of i_d is 0 independent of frequency, but the QS 40/60 model shows that the out-of-phase component of i_d is proportional to ω as shown in Table II. But this paper and CODECS show that the out-of-phase component increases in magnitude with frequency for frequencies up to the 3-dB frequency ω_{3dB} and decreases in magnitude with frequency beyond the 3-dB frequency and goes asymptotically to 0 at very high frequencies. The 3-dB frequency of this paper, ω_{3dB}, is defined to be the angular frequency where the amplitude of i_d drops to 3 dB below the dc ($\omega = 0$) value and it can be found from the amplitude plot as

$$\omega_{3dB} = 5.67 \cdot \omega_T. \quad (18)$$

In both the in-phase and the out-of-phase components of i_d, the QS 40/60 model matches this paper closely with error less than 5% for $\omega < \omega_T$.

Since an ac signal is applied only at the gate node and dc voltages are applied at all other nodes in this example, the extrinsic ac drain current flows only through the overlap capacitor between drain and gate nodes. To eliminate these extrinsic current components in the CODECS [1] simulation, the ac drain currents in the accumulation region are calculated from another CODECS simulation and are subtracted from the ac drain currents computed in the saturation region.

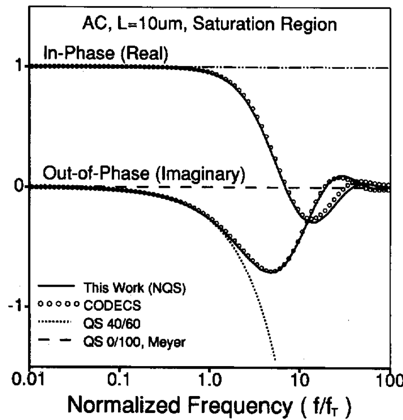

Fig. 1. In-phase (real) and out-of-phase (imaginary) components of the ac small-signal drain current i_d in the saturation region with respect to the normalized frequency f/f_T for this work, CODECS [1], the QS 40/60 and 0/100 models, and the Meyer model. Relevant equations are shown in (13.a) and (14.a). AC signal is applied at the gate node.

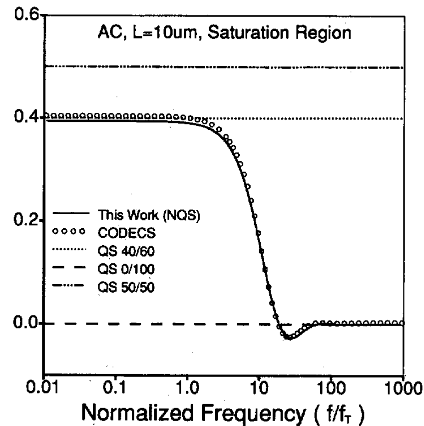

Fig. 2. The ac small-signal channel current partitioning ratio (eq. (19)) with respect to the normalized frequency (f/f_T), for this work, CODECS [1], and the QS 40/60, 50/50, and 0/100 models.

TABLE II
AC Small-Signal Drain and Source Currents i_d' and i_s' for Each Model in the Saturation Region (ω_T(QS models) = $(\mu_0 \cdot (V_{GS} - V_{TH})/L^2$. i_d and i_s are Normalized by the DC ($\omega = 0$) Value $\beta_p p_s$

	$\frac{i_d}{\beta_p p_s}$	$\frac{i_s}{\beta_p p_s}$
This Paper (non-QS)	(13.a), (14.a)	(13.b), (14.b)
QS 40/60	$1 - j \cdot \frac{4}{15} \cdot \frac{\omega}{\omega_T}$	$-1 - j \cdot \frac{2}{5} \cdot \frac{\omega}{\omega_T}$
QS 0/100	1	$-1 - j \cdot \frac{2}{3} \cdot \frac{\omega}{\omega_T}$
Meyer	1	$-1 - j \cdot \frac{2}{3} \cdot \frac{\omega}{\omega_T}$

Hence this work and CODECS give results which agree with the physical insight as follows. In the saturation region, $p(y', \omega)$ (ac small-signal phasor of $P(y, t)$ shown in (3)) at the very low frequency range ($\omega << \omega_T$) is reduced to a linear profile ($p_s(1 - y')$) and $p(y', \omega)$ at the high frequency range ($\omega >> \omega_T$) is reduced to an exponential tail ($p_s e^{-\alpha y'}$) which is nonzero only near the source end [24], due to the inertia of channel carriers which is implied in the diffusion-like equation (1.a). Since the ac channel current is proportional to the gradient of $p(y', \omega)$ with respect to y', the in-phase part of ac drain current is constant for $\omega << \omega_T$ and it goes to 0 for $\omega >> \omega_T$. Also, this paper and CODECS predict that the out-of-phase component of ac drain current increases in magnitude with frequency due to the QS capacitance effect in the low and medium frequency ranges and it goes to 0 at high frequency range. But all the QS models do not consider this non-QS inertia effect, in-phase component is constant independent of frequency, and the out-of-phase component is either 0 (QS 0/100) or increases indefinitely in proportional to ω (QS 40/60), depending on the channel charge partitioning ratio. This indefinite increase of the out-of-phase component of AC drain current with frequency for the QS 40/60 model is clearly unphysical, as pointed out by Paulos *et al.* [9].

C. AC Small-Signal Channel Current Partitioning Ratio in the Saturation Region

The ac small-signal channel current partitioning ratio, δ, is defined to be the ratio of imaginary (out-of-phase) components of the small-signal drain and source currents, i_d and i_s.

$$\delta(\omega) = \frac{\text{Im}\,(i_d(\omega))}{\text{Im}\,(i_d(\omega)) + \text{Im}\,(i_s(\omega))} \tag{19}$$

The imaginary parts of i_d and i_s for the QS models can be derived from

$$\text{Im}\,(i_d(\omega)) = \omega \cdot q_d(\omega) \tag{20.a}$$

$$\text{Im}\,(i_s(\omega)) = \omega \cdot q_s(\omega) \tag{20.b}$$

where ω is the signal angular frequency and q_d and q_s are the ac small-signal phasors for the drain and source charges, respectively. Substituting (20.a) and (20.b) into (19) and observing that the ratio between q_d and q_s becomes equal to the ratio between the total QS drain and source charges for the QS models in the saturation region, one can find that the ratio defined in (19) matches exactly the channel charge partitioning ratio for the QS models in the saturation region. The ratio is 0.4 for the QS 40/60 model, 0.0 for the QS 0/100 model, and 0.5 for the QS 50/50 model, respectively. Fig. 2 shows the ac small-signal channel current partitioning ratios with respect to the normalized frequency for this work, CODECS [1], and the QS models. Equations. (13.a) and (13.b) are used to find the partitioning ratio of this work. For the CODECS simulation, the same long channel MOSFET as in Fig. 1 is used. Excellent agreements can be observed be-

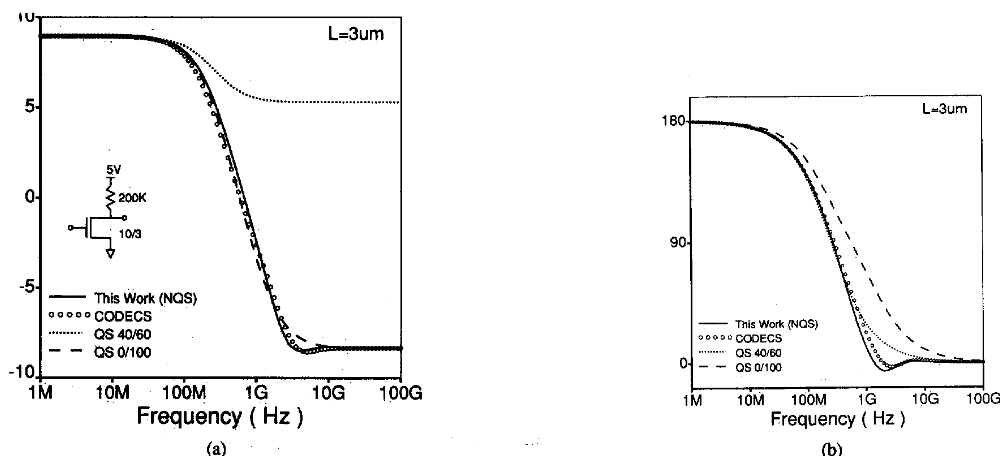

(a) (b)

Fig. 3. The frequency response of an NMOS inverter (common-source amplifier) with a resistive load and with extrinsic capacitances (overlap and junction capacitance). (a) Amplitude response ($20 \cdot \log_{10}(v_{out}/v_{in})$) (b) Phase response ($180/\pi \cdot phase_angle\,(v_{out}/v_{in})$). v_{out} and v_{in} are ac small-signal phasors for drain and gate node voltages, respectively, in this example.

TABLE III

AC Voltage Gain of an nMOS Inverter (Common Source Amplifier) with a Resistive Load in the Insert of Fig. 3(a). The Overlap Capacitance (C_{OVD}) and the Source, Drain Junction Capacitor (C_L) are Included. g_L is the Conductance of the Output Load Resistor

	$\frac{v_{out}}{v_{in}}$	$\frac{v_{out}}{v_{in}}$ (high freq.)
This paper (NQS)	$-\frac{\frac{\partial i_d}{\partial v_g} - sC_{OVD}}{g_{ds} + g_L + s(C_{OVD} + C_L)}$	$\frac{C_{OVD}}{C_{OVD} + C_L}$
QS 40/60	$-\frac{g_m - s\left(C_{OVD} + \frac{4}{15} WLC_{OX}\right)}{g_{ds} + g_L + s(C_{OVD} + C_L)}$	$\frac{C_{OVD} + \frac{4}{15} WLC_{OX}}{C_{OVD} + C_L}$
QS 0/100	$-\frac{g_m - sC_{OVD}}{g_{ds} + g_L + s(C_{OVD} + C_L)}$	$\frac{C_{OVD}}{C_{OVD} + C_L}$
Meyer	$-\frac{g_m - sC_{OVD}}{g_{ds} + g_L + s(C_{OVD} + C_L)}$	$\frac{C_{OVD}}{C_{OVD} + C_L}$

tween this work and CODECS. The partitioning ratios of this paper and CODECS are almost the same as that of the QS 40/60 model at low frequencies and go asymptotically to that of the QS 0/100 model at very high frequencies. But all the QS models show that the partitioning ratio is constant independent of frequency.

IV. Simulation Results and Comparison with Other Models

A. *Frequency Response of an nMOS Inverter with a Resistive Load*

To see the frequency response of an nMOSFET, an nMOS inverter with a resistive load is simulated using this work, CODECS [1], and the QS 40/60 and 0/100 models. This circuit is a common source amplifier. For the QS 0/100 and 40/60 models, the Berkeley Short Channel IGFET Model (BSIM) [25] implemented in SPICE3 is used. The equations for the ac voltage gain are shown in Table III for hand calculations. Extrinsic capacitances such as overlap capacitance (C_{OVD}) and junction capacitance (C_L) are included.

Fig. 3(a) and 3(b) shows the frequency response of the NMOS inverter. The effective channel length of the nMOSFET is 3 μm.

Although due to extrinsic capacitances (C_{OVD} and C_L), errors between models are smeared out and are not as clear as in intrinsic cases shown in Fig. 1, appreciable errors can still be observed between this paper and QS models. At high frequencies, the QS 40/60 model gives too large amplitude error and the QS 0/100 model gives too large phase error. The error in the phase margin of the QS 0/100 model is about 40 deg in this example.

For the CODECS simulation, 36 × 19 rectangular grids

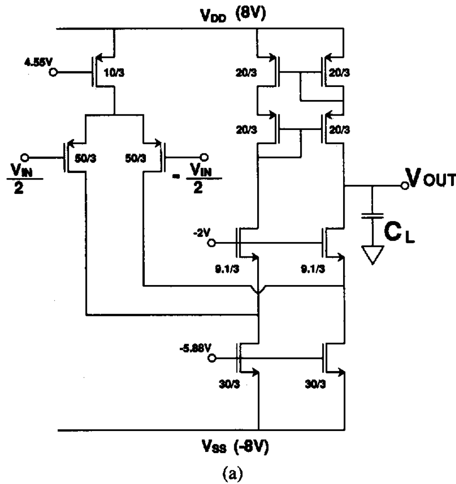

(a)

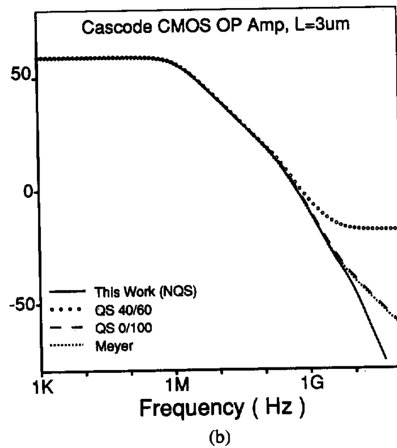

(b)

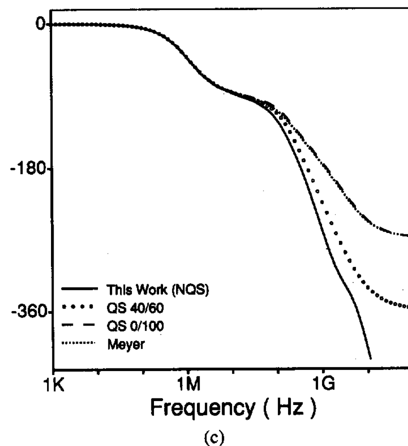

(c)

Fig. 4. Frequency response of a folded-cascode CMOS op amp [26]. Frequency compensation is not done ($C_L = 0$) to see the difference more clearly. The differential input voltage is applied to see the differential mode voltage gain. The model parameters for nMOSFET and pMOSFET of this example are shown in the nMOS2 and pMOS columns, respectively, of Table IV. The overlap capacitances of MOSFET's at drain and source sides are calculated by multiplying the channel width by *cgdo* and *cgso*, respectively. (a) Circuit diagram of a folded-cascode CMOS opamp. (b) Amplitude response of the folded-cascode CMOS opamp in Fig. 4(a). (c) Phase response of the folded-cascode CMOS opamp in Fig. 4(a).

TABLE IV
MODEL PARAMETERS USED IN THIS WORK (NQS MODEL)

	NMOS1	NMOS2	PMOS	[unit]
V_{FB}	−0.72	−0.77	−0.22	[V]
T_{OX}	50	50	50	[nm]
N_{SUB}	$2 \cdot 10^{16}$	$2 \cdot 10^{16}$	$6 \cdot 10^{15}$	[cm^{-3}]
μ_0	560	500	180	[$cm^2/(V \cdot sec)$]
cgdo	145	150	150	[pF/m]
cgso	145	150	150	[pF/m]
λ	0	0.03	0.05	[V^{-1}]
cj	471	0	0	[$\mu F/m^2$]
cjsw	94	0	0	[pF/m]

are used, and the one carrier simulation with constant mobility is used. The gate oxide thickness is set to 50 nm, the source, drain junction depths are set to 0.2 μm, the substrate doping is set to $2 \cdot 10^{16}$ cm^{-3}, and a shallow layer with the doping concentration of $1 \cdot 10^{16}$ cm^{-3} and with the thickness of 0.05 μm has been added just below the gate at the silicon region for the threshold voltage adjustment. Model parameters used for this work in Fig. 3(a) and 3(b) are shown in the nMOS1 column of Table IV.

B. Frequency Response of a Folded-Cascode CMOS opamp

Fig. 4(a) shows the circuit diagram of a folded-cascode CMOS opamp, which is widely used for its good high frequency performance and good stability characteristics [26]. Each transistor has a drawn channel length of 3 μm, and the effective channel length is 2.2 μm. Two input pMOSFET's (50 μm/3 μm) and two output nMOSFET's (9.1 μm/3 μm) form the cascode configuration and all other MOSFET's form the current sources. The differential input voltage is used to see the differential mode voltage gain.

The frequency response of the opamp in Fig. 4(a) before the frequency compensation ($C_L = 0$) is shown in Fig. 4(b) and 4(c). Overlap and junction capacitances are included in the simulation. Two pole characteristics can be observed at the frequency range less than 1 GHz. At low frequencies good agreements among all four models are observed but beyond the nondominant *pole* frequency, appreciable differences among models can be observed. The dc gain is about 60 dB, the dominant *pole* frequency is 1.1 MHz, and the nondominant pole frequency is between 200 and 300 MHz. For this paper, $f_T(\omega_T/2\pi)$ is about 180 MHz for the two input pMOSFET's and 730 MHz for the two cascode output nMOSFET's.

The amplitudes of this work, the Meyer and QS 0/100 models go to 0 at very high frequencies, but that of the QS 40/60 model goes asymptotically to a nonzero constant value, as shown in Fig. 4(b). The phase shift of this work increases unboundedly with frequency, while that of the Meyer and QS 0/100 models go to (-1.5π) radian and that of the QS 40/60 model goes to (-2π) radian due to the 2-*pole*-1-*zero* and 2-*pole*-2-*zero* characteristics, respectively. In comparison with this work, the QS 40/60

TABLE V
CPU TIME IN SPICE3(VAX 8800 WITH ULTRIX V2.0) FOR THE AC ANALYSIS OF THE FOLDED-CASCODE CMOS OPAMP IN FIG. 4(a). THE TOTAL NUMBER OF FREQUENCY POINTS IN THE SIMULATION IS 181

Model	This Paper	QS 40/60	QS 0/100	Meyer
CPU time (s)	3.2	1.6	1.6	1.5

model shows a large amplitude error and the QS 0/100 and Meyer models show large phase errors at high frequencies, respectively.

CPU time for the SPICE3 simulation is shown in Table V. This work takes about twice as long as the currently available QS SPICE3 MOSFET models in the ac analysis.

V. CONCLUSION

Based on the approximate solution of the current continuity equation, an analytic non-QS long channel MOSFET model for ac analysis has been derived and implemented in SPICE3. This model is based on the charge sheet formulation [27], and it includes both the drift and the diffusion current components. The mobility is assumed to be constant, and the NQS behavior of the bulk current is not included. The initial stage of model derivation steps of this paper is the same as that of the counterpart of this paper for transient analysis [2], and it is not repeated here to save space.

To check the validity of the model, this work has been compared with CODECS [1] (a mixed device and circuit simulator) and QS models (BSIM [25] and the Meyer model). Excellent agreements have been observed between this paper and CODECS. This paper agrees very well with QS models at low frequencies, but significant errors of QS models have been observed at high frequencies.

The frequency response of the ac small-signal channel current partitioning ratio is investigated. This ratio is exactly the same as the channel charge partitioning ratio for QS models in the saturation region. The ratio between ac drain and source currents in the saturation region is 40/60 at low frequencies and is 0/100 at high frequencies for this work and CODECS. This ratio is constant, independent of frequency for the QS models, of course.

Simulation results are presented for an NMOS inverter and a folded cascode CMOS opamp. The QS 40/60 model gives a large amplitude error, and the QS 0/100 and Meyer models give large phase error at high frequencies. So neither of these QS models is satisfactory for ac analysis at frequencies that are high relative to the inverse of the channel transit time, while this work resolved all these shortcomings of the QS models.

The CPU time required for this work is about twice as long as those for the QS models currently available in SPICE3.

This model has been applied to the transient analysis, which was published elsewhere [2], [28]. Also this NQS ac model has been combined with the SPICE level-2 dc model [29] and has been implemented in SPICE3 [30], [31]. In [31], the drain saturation voltage V_{DSSAT} of this work is replaced by V_{DSSAT} computed from the SPICE level-2 dc model. In this way all the short channel effects, such as the velocity saturation effect, the V_{GS} dependence of mobility and all other aspects considered by the level-2 dc model, were also included in the implementation. It is true that while the dc model included all these short channel effects, the ac model is still based on the long channel theory. This compromise should be judged in the light of the fact that all the currently available capacitance models in SPICE (Meyer, Ward–Dutton, BSIM) do not include any short channel effects, either, and the only shared parameters between dc and ac models are V_{TH} and V_{DSSAT}.

APPENDIX I
FIELD DEPENDENCE OF MOBILITY

In this paper, the mobility μ_0 is assumed to be constant. However, this restriction can be relieved by adding a field dependent mobility model to the final model equations. The following shows the feasibility of this paper's being extended to incorporate the field dependent mobility model. For this purpose, μ_0 in (4.c), (9.a), (9.b) and (10.b) is replaced by μ_0', which is calculated by following the scheme shown in [27], such that

$$\mu_0' = \frac{\mu_{n0}}{1 + \dfrac{\mu_{n0}(\Psi_{SL} - \Psi_{SO})}{v_{\mathrm{SAT}} L}} \tag{A1.1}$$

where

$$\mu_{n0} = \frac{\mu_0}{1 + \dfrac{E_{\mathrm{eff}}}{E_{\mathrm{CRIT}}}} \tag{A1.2}$$

$$E_{\mathrm{eff}} = \frac{C_{\mathrm{OX}}}{\epsilon_s} \cdot (0.5 \cdot V_{\mathrm{GST}} + \gamma \sqrt{\Psi_{\mathrm{SO}} - V_t}) \tag{A1.3}$$

where v_{SAT}, μ_0, and E_{CRIT} are model parameters for maximum drift velocity, zero field mobility, and critical vertical electric field for mobility degradation, respectively. (A1.1) models the horizontal field dependence of mobility (drift velocity saturation effect) and (A1.2) models the vertical field dependence of mobility (surface scattering effect). (A1.2) does not conflict with the assumption of constant mobility along the channel length direction which is used in deriving eq. (8) of [2]. But (A1.1) assumes the y dependence in its derivation step [27] and does conflict with the constant mobility assumption. Hence, the drift velocity saturation effect (y dependence of mobility) is not incorporated during the derivation of model equations, but the effect is added to the final model equations in an *ad hoc* manner.

To see the effect of the field dependent mobility on the ac node currents, two CODECS simulations were done for an nMOSFET, one for constant mobility and the other for field dependent mobility, and the comparisons are shown in Fig. 5. Apparently the two simulation results

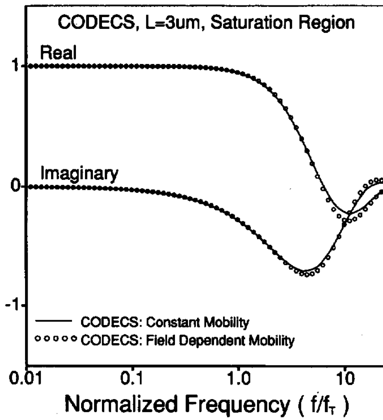

Fig. 5. Comparison of two CODECS simulations (one for constant mobility and the other for field dependent mobility) to see the effect of mobility variation on ac node currents. The nMOSFET used is the same as that in Fig. 3. $V_G = 3$ V, $V_D = 5$ V, $V_B = 0$, and $V_S = 0$. ac signal is superimposed at the gate node.

TABLE VI
COMPARISON OF f_T AND NORMALIZATION FACTORS FOR THE TWO CODECS SIMULATIONS SHOWN IN FIG. 5

Mobility model	f_T (GHz)	Normalization factor (μA/V)
Constant mobility	2.24	162.2
Field dependent mobility	1.18	109.3

are much different from each other as shown in Table VI. After normalization, good agreements are achieved between the two simulation results as shown in Fig. 5. Hence, in this example, the field dependent mobility brought the changes only in dc value and the shift in f_T.

APPENDIX II
EQUATIONS FOR COEFFICIENTS $b_1(\omega)$, $b_2(\omega)$, $d_1(\omega)$, $d_2(\omega)$, $G(\omega)$, AND $H(\omega)$

The coefficients $b_1(\omega)$, $b_2(\omega)$, $d_1(\omega)$ and $d_2(\omega)$ are asymmetry terms and can be found by substituting (5) into (4.a) and matching $p(0, \omega)$ and the integrated $p(y', \omega)$ from $y' = 0$ to $y' = 1$ in both sides of the equation. Hence

$$b_1(\omega) = \frac{-B}{C - E \cdot \alpha(\omega)} \tag{A2.1}$$

$$b_2(\omega) = -\alpha(\omega) \cdot b_1(\omega) \tag{A2.2}$$

$$d_1(\omega) = \frac{-B}{C + E \cdot \alpha(\omega)} \tag{A2.3}$$

$$d_2(\omega) = \alpha(\omega) \cdot d_1(\omega) \tag{A2.4}$$

$$B = r^2 \left\{ r - \frac{2}{3}(1 - (1 - r)^{1.5}) \right\} \tag{A2.5}$$

$$C = 3r \left\{ \frac{2}{3}(1 - (1 - r)^{1.5}) - \frac{2}{5}(1 - (1 - r)^{2.5}) \right\} + 0.5r^3 \tag{A2.6}$$

$$E = \frac{r^3}{3} - \frac{2}{3}(1 - (1 - r)^{1.5}) + \frac{4}{5}(1 - (1 - r)^{2.5}) - \frac{2}{7}(1 - (1 - r)^{3.5}). \tag{A2.7}$$

Coefficients B, C, and E are real positive constants at a given dc operating point. Coefficients $b_1(\omega)$, $b_2(\omega)$, $d_1(\omega)$, and $d_2(\omega)$ go to 0 asymptotically as r goes to 0. From the two boundary values of the phasor profile $p(y', \omega)$ at the source and drain ends, $p_s(\omega)$ and $p_d(\omega)$, we can find the coefficients $G(\omega)$ and $H(\omega)$.

$$G(\omega) = \frac{p_s(\omega) \cdot (1 + d_1(\omega) + d_2(\omega)) \cdot e^{-\alpha(\omega)} - p_d(\omega)}{(1 + d_1(\omega) + d_2(\omega)) \cdot e^{-\alpha(\omega)} - (1 + b_1(\omega) + b_2(\omega)) \cdot e^{\alpha(\omega)}} \tag{A2.8}$$

$$H(\omega) = \frac{p_d(\omega) - p_s(\omega) \cdot (1 + b_1(\omega) + b_2(\omega)) \cdot e^{\alpha(\omega)}}{(1 + d_1(\omega) + d_2(\omega)) \cdot e^{-\alpha(\omega)} - (1 + b_1(\omega) + b_2(\omega)) \cdot e^{\alpha(\omega)}}. \tag{A2.9}$$

REFERENCES

[1] K. Mayaram, "CODECS: A mixed-level circuit and device simulator," Memo. UCB/ERL M88/71, Electronics Research Lab., Univ. California, Berkeley, Nov. 1988.

[2] H. J. Park, P. K. Ko, and C. Hu, "A non-quasi-static MOSFET model for SPICE-transient analysis," *IEEE Trans. Electron Devices*, vol. 36, pp. 561-576, Mar. 1989.

[3] D. A. Hodges, P. R. Gray, and R. W. Brodersen, "Potential of MOS technologies for analog integrated circuits," *IEEE J. Solid State Circuits*, vol. SC-13, pp. 285-294, June 1978.

[4] J. E. Meyer, "MOS models and circuit simulation," *RCA Rev.*, vol. 32, pp. 42-63, 1971.

[5] S. Y. Oh, D. E. Ward, and R. W. Dutton, "Transient analysis of MOS transistors," *IEEE J. Solid State Circuits*, vol. SC-15, pp. 636-643, Apr. 1980.

[6] D. E. Ward and R. W. Dutton, "A charge-oriented model for MOS transistor capacitances," *IEEE J. Solid State Circuits*, vol. SC-13, pp. 703-708, June 1978.

[7] P. Yang and P. K. Chatterjee, "SPICE modelling for small geometry MOSFET circuits," *IEEE Trans. Computer-Aided Design*, vol. CAD-1, pp. 169-182, 1982.

[8] H. Khorramabadi and P. R. Gray, "High-frequency CMOS continuous time filters," *IEEE J. Solid State Circuits*, vol. SC-19, pp. 939-948, Dec. 1984.

[9] J. J. Paulos and D. A. Antoniadis, "Limitations of quasi-static capacitance models for the MOS transistor," *IEEE Electron Device Lett.*, vol. EDL-4, pp. 221-224, 1983.

[10] M. Bagheri and Y. P. Tsividis, "A small signal dc-to-high frequency nonquasistatic models for the four-terminal MOSFET valid in all regions of operation," *IEEE Trans. Electron Devices*, ED-32, pp. 2383-2391, Nov. 1985.

[11] C. Turchetti, P. Mancini, and G. Masetti, "A CAD-oriented nonquasistatic approach for the transient analysis of MOS IC's," *IEEE J. Solid State Circuits*, vol. SC-21, pp. 827-836, 1986.

[12] P. Mancini, C. Turchetti, and G. Masetti, "A non-quasi-static analysis of the transient behavior of the long channel MOST valid in all regions of operation," *IEEE Trans. Electron Devices*, vol. 34, pp. 325-334, Feb. 1987.

[13] J. G. Fossum, H. Jeong, and S. Veeraraghavan, "Significance of the channel-charge partition in the transient MOSFET model," *IEEE Trans. Electron Devices*, vol. ED-33, pp. 1621-1623, Oct. 1986.

[14] M. F. Sevat, "On the channel charge division in MOSFET modeling," *Tech. Dig. ICCAD*, pp. 208-210, Nov. 1987.

[15] J. R. Burns, "High frequency characteristics of the insulated gate field effect transistor," *RCA Rev.*, pp. 385-418, Sept. 1967.

[16] M. B. Das, "High frequency network properties of MOS transistors including the substrate resistivity effects," *IEEE Trans. Electron Devices*, vol. ED-16, pp. 1049-1069, Dec. 1969.

[17] D. H. Treleaven, and F. N. Trofimenkoff, "MOS FET equivalent

circuit at pinch-off," *Proc. IEEE*, vol. 54, pp. 1223–1224, Sept. 1966.

[18] P. Roblin, S. C. Kang, and H. Morkoc, "Analytic solution of the velocity-saturated MOSFET/MODFET wave equation and its application to the prediction of the microwave charactersitics of MODFET's," *IEEE Trans. Electron Devices*, vol. 37, pp. 1608–1622, July 1990.

[19] H. C. Poon, "V*th* and beyond," presented at the Workshop on Device Modeling for VLSI, Burlingame, CA, March 1979.

[20] H. I. Hanafi, "3.1 current modeling for MOSFET," *Circuit Analysis, Simulation and Design*, Part 1, A. E. Ruehli, Editor. New York: North Holland, 1986, pp. 98–99.

[21] B. J. Sheu, "MOS transistor modeling and characterization for circuit simulation," Electronics Research Lab., Univ. of California, Berkeley, Memo. UCB/ERL M85/85, Oct. 1985.

[22] Y. P. Tsividis, *Operation and Modeling of the MOS Transistor*. New York: McGraw-Hill, 1987.

[23] H. J. Park, P. K. Ko, C. Hu, "A non-quasistatic MOSFET model for SPICE," in *Int. Electron Devices Meeting 87 Tech. Dig.*, Dec. 1987, pp. 652–655.

[24] H. J. Park, "Charge sheet and non-quasistatic MOSFET models for SPICE," Ph.D. dissertation, Electron. Res. Lab., Dept. of EECS, University of California, Berkeley, Memo. UCB/ERL M89/20, Feb. 1989.

[25] B. J. Sheu, D. L. Scharfetter, P. K. Ko, and M. C. Jeng, "BSIM: Berkeley short channel IGFET model for MOS transistors," *IEEE J. Solid-State Circuits*, vol. 22, pp. 558–566, Aug. 1987.

[26] P. R. Gray and R. G. Meyer, "MOS operational amplifier design—A tutorial overview," *IEEE J. Solid-State Circuits*, vol. SC-17, pp. 969–982, Dec. 1982.

[27] H. J. Park, P. K. Ko, and C. Hu, "A charge sheet capacitance model for short channel MOSFET's for SPICE," *IEEE Trans. Computer-Aided Design*, vol. 10, pp. 376–389, Mar. 1991.

[28] —, "A charge-conserving non-quasi-static (NQS) MOSFET model for SPICE transient analysis," *IEEE Trans. Computer-Aided Design*, vol. 10, pp. 629–642, May 1991.

[29] A. Vladimirescu and S. Liu, "The simulation of MOS integrated circuits using SPICE2," Electron. Res. Lab., Dept. of EECS, Univ. California, Berkeley, Memo. UCB/ERL M80/7, Oct. 1980.

[30] T. L. Quarles, A. R. Newton, D. O. Pederson, and A. Sangiovanni-Vincentelli, "SPICE 3B1 User's Guide," Electron. Res. Lab., Univ. California, Berkeley, Nov. 1987.

[31] H. J. Park, P. K. Ko, and C. Hu, "SPICE3 implementation of a non-quasi-static MOSFET model with level-2 dc model," Electron. Res. Lab., Univ. California, Berkeley, Memo. UCB-ERL M89/70, June 1989.

Hong-June Park (S'84–M'88) received the B.S. degree in electronics engineering from Seoul National University in 1979, the M.S. degree in electrical engineering from K.A.I.S.T., Seoul, Korea, in 1981, and the Ph.D. degree in electrical engineering and computer sciences from University of California, Berkeley, in 1989. His Ph.D. dissertation deals with charge-sheet and non-quasi-static MOSFET charge and capacitance models for SPICE.

From 1981 to 1984, he was a research staff member in the Design Automation Laboratory, Electronics Telecommunication Research Institute, Daejun, Korea, where he worked on SPICE MOSFET model parameter extraction system. From 1989 to 1991, he was a Senior Engineer at Technology CAD, INTEL, Santa Clara, CA, where he worked on the MOSFET and BJT model parameter extraction and circuit simulation programs. Since 1991 he has been with the Department of Electrical Engineering, Pohang Institute of Science and Technology, where he is an Assistant Professor. His research interests include semiconductor device modeling for SPICE, interconnect and package modeling, and ASIC design.

Dr. Park is a member of KIEE.

Ping Keung Ko (S'78–M'81) received the B.S. degree in physics with special honors from Hong Kong University, and the M.S. and Ph.D. degrees in electrical engineering from the University of California at Berkeley, in 1978 and 1982, respectively.

In 1982 and 1983, he was a Member of the Technical Staff at Bell Laboratories, Holmdel, NJ, where he was responsible for the development of high-speed MOS technologies for communication circuits. He joined the Berkeley faculty in 1984, where he is now a Professor of electrical engineering and computer sciences. His present research interests include high-speed VLSI technologies and devices, device modeling for circuit simulation, and electronic neural network. He has authored or co-authored one book and over 100 research papers. Currently, he is the director of the Berkeley Microfabrication Laboratory.

Dr. Ko has served on the program committees of the International VLSI Technology Symposium and the International Electron Device Meeting. He has also been Associate Editor of IEEE TRANSACTIONS ON ELECTRON DEVICES since March 1988.

Chenming Hu (S'71–M'76–SM'83–F'90) received the B.S. degree from the National Taiwan University and the M.S. and Ph.D. degrees in electrical engineering from the University of California, Berkeley, in 1970 and 1973, respectively.

From 1973 to 1976 he was an Assistant Professor at Massachusetts Institute of Technology, Cambridge, MA. In 1976 he joined the University of California, Berkeley, as Professor of electrical engineering and computer sciences. He is Director of the Joint Services Electronics Program at Berkeley. While on industrial leave from the University in 1980–81 he was Manager of Nonvolatile Memory Development at National Semiconductor. Since 1973 he has served as a consultant to the electronics industry. He has also been an advisor to many government and educational institutions. His present research areas include VLSI devices, including silicon-on-insulator devices, hot electron effects, thin dielectrics, electromigration, circuit reliability simulation, and nonvolatile semiconductor memories. He has also conducted research on electro-optics, solar cells, and power electronics. He has been awarded several patents on semiconductor devices and technology. He has authored or coauthored three books and over 250 research papers. He has delivered a dozen keynote addresses and invited papers at scientific conferences, and has received five best paper awards. He is an Honorary Professor of Beijing University and Tsinghua University, China, and of the Chinese Academy of Science. He was associate editor of IEEE TRANSACTIONS ON ELECTRON DEVICES from 1986 to 1988 and Vice Chairman of IEEE Electron Devices Society, Santa Clara Valley Chapter, 1980–1982. He was appointed the first National Science Council Invited Chair Lecturer, Republic of China, in 1987. He was Board Chairman of the East San Francisco Bay Chinese School from 1988 to 1991. He received the 1991 *Design News* Excellence in Design Award for leading the development of an IC Reliability Simulator, BERT.

Dr. Hu has been listed in *American Men and Women of Science*, *Who is Who in Science and Engineering*, and *Who's Who in American Education*.